

High-resolution spectroscopy of the young open cluster M 39 (NGC 7092)

J. Alonso-Santiago¹, A. Frasca¹, G. Catanzaro¹, A. Bragaglia², L. Magrini³, A. Vallenari⁴, E. Carretta², and S. Lucatello⁴

¹ INAF–Osservatorio Astrofisico di Catania, via S. Sofia 78, 95123 Catania, Italy

² INAF–Osservatorio di Astrofisica e Scienza dello Spazio, via P. Gobetti 93/3, 40129 Bologna, Italy

³ INAF–Osservatorio Astrofisico di Arcetri, Largo E. Fermi 5, 50125 Firenze, Italy

⁴ INAF–Osservatorio Astronomico di Padova, vicolo dell’Osservatorio 5, 35122 Padova, Italy

ABSTRACT

M 39 is a nearby young open cluster hardly studied in the last decades. No giant is known among its members and its chemical composition has never been studied. In order to investigate it we performed high-resolution spectroscopy of 20 expected cluster members with the HARPS and FIES spectrographs. By combining our observations with archival photometry and *Gaia*-DR3 data we searched for evolved members and studied cluster properties such as the radial velocity, extinction and age. For the first time, we provide stellar parameters and chemical abundances for 21 species with atomic numbers up to 56. We have not found any new giant as likely member and notice a negligible reddening along the cluster field, that we place at 300 pc. We obtain a mean radial velocity for M 39 of $-5.5 \pm 0.5 \text{ km s}^{-1}$ and an isochrone-fitting age of $430 \pm 110 \text{ Ma}$, which corresponds to a MSTO mass of around $2.8 M_{\odot}$. This value is consistent with the Li content and chromospheric activity shown by its members. Based on main-sequence stars the cluster exhibits a solar composition, $[\text{Fe}/\text{H}] = +0.04 \pm 0.08 \text{ dex}$, compatible with its Galactocentric location. However, it has a slightly subsolar abundance of Na and an enriched content of neutron-capture elements, specially Ba. In any case, the chemical composition of M 39 is fully compatible with that shown by other open clusters that populate the Galactic thin disc.

Key words. open clusters and associations: individual: M 39 – open clusters and associations: individual: NGC 7092 – Hertzsprung-Russell and C-M diagrams – stars: abundances – stars: fundamental parameters

1. Introduction

The abundance and spatial distribution of the different chemical elements as well as their variation over time, are keys to understanding the origin and evolution of our Galaxy. In the era of *Gaia* and the large spectroscopic surveys, such as for example *Gaia*-ESO (Gilmore et al. 2022; Randich et al. 2022), GALAH (De Silva et al. 2015) and APOGEE (Majewski et al. 2017), Galactic Archaeology is experiencing an unprecedented advance, significantly improving our knowledge of the structures and history of the Milky Way. Open clusters (OCs) are among the best tracers of the Galactic thin disc, since they are disseminated throughout it, covering a wide range of distances and ages. Furthermore, the chemical cluster composition, usually based on the analysis of a large number of members, is more reliable than that obtained from individual field stars. The best tool for deriving accurate chemical abundances is high-resolution spectroscopy. However, despite these large surveys and some other that are about to come into operation like WEAVE (Jin et al. 2023) and 4MOST (de Jong et al. 2019), only a small fraction of OCs (around 10%) have been observed in this way to date. This fraction could be even lower if we consider the recently discovered new OCs (Hunt & Reffert 2023) in light of the *Gaia* third data release (*Gaia*-DR3, *Gaia* Collaboration et al. 2022). Thus, high-resolution spectroscopy, such as the one conducted in this work, is highly required to continue studying our Galaxy in depth.

M 39 (also known as NGC 7092) is a sparse and nearby OC in Cygnus. It was first studied by Trumpler (1928), who classi-

fied it as a type Ia object. That means the cluster hosts only main sequence (MS) stars, i.e. with no late-type giants, not earlier than spectral type A. The most relevant works focused on M 39 date back several decades (see e.g., Ebbighausen 1940; Eggen 1951; Johnson 1953; Weaver 1953; Abt & Sanders 1973; Abt & Levato 1976; McNamara & Sanders 1977; Mohan & Sagar 1985; Manteiga et al. 1991; Platais 1994). The cluster has been mostly studied by combining photographic and photoelectric *UBV* photometry, spectral types obtained with low-resolution slit spectroscopy and membership identification based on proper motions derived from photographic plates. These works determined the cluster properties by observing a small number of stars, a few dozens at best. Nonetheless, Platais (1994) provided photometry and proper motions for 7931 stars in the field of M 39, assigning spectral types for 511 of them.

The aforementioned studies agree that the cluster lies at around 300 pc and that is practically unaffected by interstellar extinction. Among the MS stars the earliest spectral type is found to be B9-A0 (e.g. Abt & Levato 1976), confirming the pioneering result of Trumpler (1928). As there is no evolved members it has not been easy to accurately determine the age of the cluster, which appears to be in the 200–500 Ma¹ range (Mohan & Sagar 1985; Manteiga et al. 1991).

Recently, Cantat-Gaudin et al. (2020), based on the *Gaia* second data release, placed M 39 at 311 pc, found no apprecia-

¹ Throughout the text we follow the recommendations of the IAU using the symbol *a* (from the Latin word *annus*) as the unit of time rather than yr.

ble reddening in the cluster field and estimated an age of about 400 Ma. To date, M 39 has not yet been observed with high-resolution spectroscopy and its chemical composition remains unknown. The main aim of this paper is to fill this gap. We conducted the present investigation using high-resolution spectra, archival photometry and *Gaia*-DR3 data with the aim of characterizing the main properties of the cluster. We payed particular attention to the determination of the chemical abundances of a large number of elements that allow us to perform the proper chemical tagging of our target. The paper is structured as follows. We present our observations in Sect. 2 and explain the search performed to identify new (evolved) cluster members in Sect. 3. Then, in Sect. 4 we describe our spectral analysis and in Sect. 5 we study the cluster reddening. The investigation of the age is outlined in Sect. 6, while the discussion and comparison of our main results with the literature are presented in Sect. 7. Finally, we summarise our results and present the conclusions of this work in Sect. 8.

2. Observations

A fundamental step when studying a stellar cluster is to carefully choose a representative sample of members. In this work the target selection was performed before the publication of the *Gaia*-DR2 catalogue. Therefore, as a starting point, we made use of the list of members identified by Platais (1994), the most comprehensive study focused on M 39 available in the literature. Then, we completed our target list taking advantage of the selection made by Cantat-Gaudin et al. (2018). As noted above, the cluster does not host any cool giants and, therefore, our sample consists of MS stars only. For this reason, we payed special attention to the brightest stars located in the upper MS and the turn-off point (TO) that can help us to constrain the cluster age.

2.1. Spectroscopy

The observations were conducted mainly in October 2017. High-resolution spectroscopy was taken for our targets by employing two different spectrographs, both located at *El Roque de los Muchachos* Observatory (La Palma, Spain). Most of the sources, 17, were observed with the High Accuracy Radial velocity Planet Searcher for the Northern hemisphere spectrograph (HARPS-N, Cosentino et al. 2014) while three other spectra were obtained with the Fibre-fed Echelle Spectrograph (FIES, Telting et al. 2014). HARPS-N is an échelle spectrograph fibre-fed from the Nasmyth B focus of the 3.6-m *Telescopio Nazionale Galileo* (TNG). It covers the wavelength range between 3900 and 6800 Å in 68 orders and provides a resolving power of $R=115\,000$. As regards FIES, it is mounted at the the 2.5-m Nordic Optical Telescope (NOT). It covers the spectral range 3700-9000 Å in 81 orders, being able to work at three different resolutions. We used the high-resolution mode, which provides a $R=67\,000$. Additionally, three other spectra were taken with HARPS-N in 2020.

The spectra were acquired with exposures times (t_{exp}) ranging from 300 to 7200 s, depending on the star brightness and sky conditions. To reduce the contamination of cosmic rays, we avoid taking exposures longer than 1800 s. A standard reduction of both sets of spectra was performed using the corresponding instrument pipeline. In total we collected 24 spectra for 20 different stars, which are listed in Table 1. Throughout this paper we follow the numbering assigned by Platais (1994) to identify our targets. The star UCAC4 683-104396, a bona fide member

Table 1. Observation log.

Star ^a	Name	Date	t_{exp} (s)	S/N ^b
HARPS-N				
0305	TIC 64397736	2017-10-03	7200	46
0305	TIC 64397736	2020-08-02	6300	53
3004	BD+47 3440	2017-10-04	3600	40
3061	TYC 3594-834-1	2017-10-29	7200	92
3288	TIC 64983141	2017-12-05	7200	76
3311	BD+47 3442	2017-10-29	3600	105
3423	TYC 3594-678-1	2017-10-04	7200	92
3781	HD 205116	2017-10-29	600	126
3814	HD 205117	2017-10-29	1200	118
4265	HD 205198	2017-10-03	1200	155
4322	TIC 417208749	2017-10-28	7200	35
4438	TYC 3598-511-1	2017-10-28	7200	47
4673	BD+47 3462	2017-10-29	1800	71
5045	HD 205331	2017-10-29	1200	174
5609	TYC 3599-2886-1	2017-10-04	2400	55
5609	TYC 3599-2886-1	2017-10-28	1200	40
5729	BD+48 3423	2017-10-03	3600	161
6791	BD+47 3480	2017-10-29	3600	131
ucac	UCAC4 683-104396	2020-09-08	4200	29
ucac	UCAC4 683-104396	2020-11-24	2100	38
FIES				
2451	HD 204917	2017-10-23	900	65
4294	HD 205210	2017-10-23	1200	100
7140	BD+47 3485	2017-10-22	300	85
7140	BD+47 3485	2017-10-24	300	60

^a Designation from Platais (1994)

^b Signal-to-noise ratio per pixel at 6500 Å.

according to Cantat-Gaudin et al. (2018) observed in our last run, is out of the field surveyed by Platais (1994). For this reason we use “ucac” as a shorthand designation for this star.

2.2. Archival data

To complement our spectroscopic observations we resorted to archival data provided by some all-sky surveys. This information will be very useful later as it will allow us to study both the cluster members and the cluster itself. On the one hand, we used photometric data in the optical range from the APASS catalogue (Henden et al. 2016) and in the near-infrared wavelengths from the 2MASS (Skrutskie et al. 2006) and WISE (Cutri & et al. 2012) catalogues. On the other hand, we took advantage of the last data release, DR3, of the *Gaia* mission (Gaia Collaboration et al. 2022). Tables A.1 and A.2 report the *Gaia*-DR3 source identifier as well as the photometric and astrometric data for the stars observed in this work at the end of the paper.

3. Cluster membership

The disentangling of cluster members from field stars is not a trivial task. However, to succeed in the characterisation of the cluster, a correct identification of its members is essential. The arrival of a large amount of high-precision photometric and, specially, astrometric data from the *Gaia* mission, has been of great help in simplifying this task.

Platais (1994) observed about 8000 stars in the field of M 39 and identified 511 likely members among them. His analysis was based on *UBV* photometry and proper motions measured on photographic plates. As above mentioned, we selected our targets from this list. Specifically, we took 19 high-probability members, that is, with an assigned membership probability, $P \geq 0.7$, among the brightest.

Cantat-Gaudin et al. (2018) taking advantage of the *Gaia*-DR2 identified 198 members, out of which 154 bona fide members (i.e. with $P \geq 0.7$) were found. Among our targets, 14 are also high-probability members according to them, while the remaining five stars, namely 3004, 3423, 4294, 5045, and 5609, are not considered by them as cluster members. In a second run, we observed the star ucac, a likely member reported in Cantat-Gaudin et al. (2018), out of the field studied by Platais (1994).

With the intention of finding new members, and specially some giant that allow us to improve the estimation of the cluster age when performing the isochrone fitting, we carried out a search around the nominal centre of the cluster. We took all the sources from the *Gaia*-DR3 catalogue brighter than $G=18$ within a radius of $250''$ around it. In total we collected $\approx 1\,250\,000$ objects with a complete set of astrometric (i. e. $\mu_{\alpha*}$, μ_{δ} , ϖ) and photometric (G , G_{BP} , G_{RP}) parameters.

Cantat-Gaudin et al. (2018) placed M 39 in the astrometric space at $(\mu_{\alpha*}, \mu_{\delta}, \varpi) = (-7.477, -19.738, 3.337) \pm (0.381, 0.393, 0.090)$ (mas, mas a⁻¹, mas a⁻¹). When updating the *Gaia* parameters from DR2 to DR3 for the members reported in that paper we noticed a non negligible dispersion in the astrometric data, but not in the photometric values (see Figs. A.1 and A.2). For this reason we decided to recalculate the cluster centre adopting the average DR3 values of their bona fide members. Thus, we now found the cluster at $(\mu_{\alpha*}, \mu_{\delta}, \varpi) = (-7.459, -19.839, 3.367) \pm (0.345, 0.419, 0.088)$, where the errors correspond to the standard deviation. Once we determined the cluster centre in the astrometric space, we adopted a radius around it of 3σ , 4σ and 5σ as a membership criterion to define three classes of members: type I (high-probability), type II (medium-probability) and type III (marginal membership), respectively. In this way, we identified 196, 48 and 27 likely members within these three radii, finding 147, 5 and 0 bona fide members from Cantat-Gaudin et al. (2018), respectively.

In a second step we refined our selection of members by means of photometry. We plotted the $(G_{BP} - G_{RP})/G$ diagram and rejected those objects (six in total) whose position on the diagram was discrepant, since they lied far away from the sequence of the cluster, that is clearly outlined. Finally, we also used the *Gaia* RV to improve our member list. As a result, five other objects have been identified as outliers and, therefore, their membership has been ruled out (see Sect. 4.1). Our final member list is composed of 260 objects, out of which 195 are considered type I, 43 belong to type II and the remaining 22 are classified as type III members. The cluster probabilities for all our targets are listed in Table A.1 and the colour-magnitude diagram is displayed in Fig. 1.

We point out that the cluster is well defined in the astrometric space and contamination from field stars is low. We have expanded the member list provided by Cantat-Gaudin et al. (2018) by about 30%, but nevertheless we have not found any giants. According to our criterion we observed 17 high-probability members among our targets, while we had to reject the stars 3004, 3423 and 4294 as cluster members. Therefore, their parameters were not used in calculating the average values of the cluster.

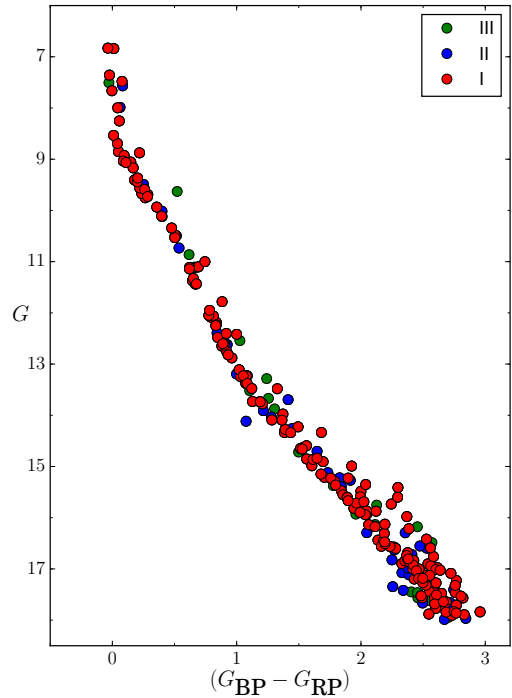


Fig. 1. *Gaia* colour-magnitude diagram of M 39 displaying the members identified in this work. The colour indicates the membership class, as defined in the text.

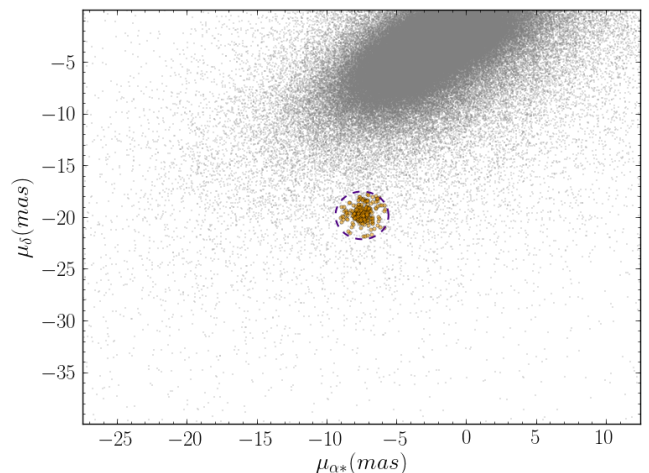


Fig. 2. Proper motion diagram in the field of M 39. The extent of the cluster in the astrometric space is delimited by the ellipse, whose semi-axes correspond to five times the uncertainty of the mean $\mu_{\alpha*}$, μ_{δ} values. Grey dots represent sources with $G \leq 16$ mag within a radius of $250''$ around the nominal cluster center.

By examining the spatial distribution of the members in the RA–DEC plane (Fig.3) we found the cluster centre by fitting a Gaussian to the histogram showing the projected distribution on each coordinate. In this way we put the cluster at $\alpha(\text{J2000}) = 21^h 31^m 23.4^s$, $\delta(\text{J2000}) = 48^\circ 11' 35.3''$, which is slightly displaced with respect to the estimate by Cantat-Gaudin et al. (2018), ours minus theirs, $\Delta(\alpha, \delta) = (-10.0^s, -3.2'')$. Likewise, from the parallaxes of the members we derived the dis-

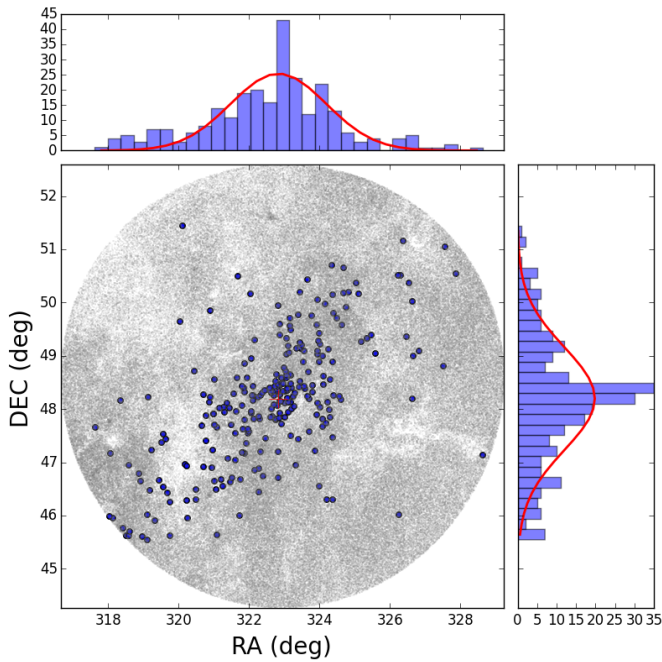


Fig. 3. Sky region around M 39. The density map represents sources with $G \leq 16$ mag within a radius of $250'$ around the nominal cluster centre while the blue circles are the members identified in this work. A histogram showing the member distribution along each axis is also displayed.

tance to the cluster. Firstly, we corrected the parallax zero-point offset for each star following the recommendations outlined by Lindegren et al. (2021). As a guide, we found that, on average, this correction was of -0.032 mas with respect to the published value. We then calculated the individual distances by inverting the corrected parallaxes and finally, the cluster value was obtained after fitting a Gaussian to the distribution of the member distances. We place the cluster at 294 ± 7 pc, where the error is the σ of the Gaussian.

4. Spectral Analysis

Before starting the spectral analysis, the telluric H_2O lines at the $\text{H}\alpha$ and NaID_2 wavelengths, as well as those of O_2 at 6300 \AA , were removed from the spectra. The same procedure described by Frasca et al. (2000) was followed. For this purpose we used telluric templates (spectra of hot, fast-rotating stars) acquired during the observing run.

4.1. Radial velocity

The first step of our analysis consists in measuring the heliocentric radial velocity (RV) of the observed objects. With this aim we cross-correlated the target spectra against synthetic templates by using the task `FXCOR` of the IRAF² package.

When examining the cross-correlation function (CCF), we note that stars 3423, 3781, and 3814 exhibit a double or a

Table 2. Radial velocities of the newly discovered SB2 systems.

Star	HJD (2 400 000+)	RV ₁ (km s ⁻¹)	RV ₂ (km s ⁻¹)
3423	58029.9742	-7.98 ± 1.47	-2.09 ± 0.69
3781	58055.0448	-24.95 ± 0.55	-3.05 ± 4.23
3814	58055.0556	9.02 ± 1.74	-76.50 ± 9.63

strongly asymmetric peak, which clearly suggests a binary nature (see Fig. A.3). However, since we have a single spectrum for each of them in which the peaks are not fully resolved, we cannot provide orbital and stellar parameters but we can only classify them as likely double-lined spectroscopic binaries (SB2s) and provide the radial velocity of their primary (more luminous) and secondary components in Table 2. For the remaining stars, considered single for all purposes, the RVs are displayed in the last column of Table 3.

With the exception of the SB2 systems and 5609 (a fast rotator), most of the stars have an RV that ranges from -6 to -3 km s^{-1} . We obtained a mean radial velocity for the cluster, $\text{RV} = -5.46 \pm 0.54$. This weighted average has been calculated using as weight $w = 1/\sigma_{\text{RV}}^2$, where σ_{RV} is the RV error of each star. The weighted standard deviation has been used to estimate the uncertainty. We compared our result with the *Gaia* RVs of our likely members, which were first identified based on astrometry and photometric criteria (Sect. 3). Among them, RV is provided for only 122 stars. We derived the cluster mean by fitting a Gaussian to the distribution of the individual values, obtaining $\text{RV} = -6.1 \pm 2.3 \text{ km s}^{-1}$. We notice that our result shows strong agreement with *Gaia* RVs. Additionally, based on these RVs, we rejected five objects as members since their values, within the errors, are beyond 5σ the cluster average (see Fig. A.4). However, we cannot exclude that these stars are indeed binary systems and the discrepant RV, compared with the cluster mean, is the result of the orbital motion.

4.2. Atmospheric parameters

The stellar atmospheric parameters of our targets, i.e. effective temperature (T_{eff}), surface gravity ($\log g$) and metallicity ($[\text{Fe}/\text{H}]$) have been determined by using the ROTFIT code (Frasca et al. 2006), tailored to our data, as already done in previous works (see e.g., Frasca et al. 2019; Alonso-Santiago et al. 2021). Additionally, ROTFIT also provides the projected rotational velocity ($v \sin i$) and the spectral type (SpT) for each star. ROTFIT works by performing a χ^2 minimisation of the difference between the target spectrum and a grid of templates. This difference is evaluated in 28 spectral segments of 100 \AA each from 4000 \AA to 6800 \AA . Then, the final parameters are calculated by averaging the results of the individual regions, weighting them according to the χ^2 and the amount of spectral information contained in each segment. The grid of templates consists of ELODIE spectra ($R = 42\,000$) of real stars with well-known parameters. It is the same grid used by the Catania node within the *Gaia*-ESO Survey (Smiljanic et al. 2014; Frasca et al. 2015). Since ROTFIT is optimised to analyse FGK-type stars, for the hottest targets we employed a different approach for which we used a grid of synthetic spectra computed as described in Sect. 4.3. For these stars we used the wings and cores of Balmer lines to determine T_{eff} and $\log g$. The $v \sin i$ was derived in a re-

² IRAF is distributed by the National Optical Astronomy Observatory, which is operated by the Association of the Universities for Research in Astronomy, Inc. (AURA), under cooperative agreement with the National Science Foundation.

gion around the $\text{Mg II } \lambda 4481$ line, while a solar metallicity was assumed as the rapid rotation of these sources makes very difficult to measure it. For more detailed information on our method, the reader is referred to Frasca et al. (2019). Results are summarized in Table 3. The metallicities reported in Table 3 have been refined by applying SYNTHE to our spectra (see Sect. 4.3) and adopting the $[\text{Fe}/\text{H}]$ values derived with ROTFIT as a starting point. However, these values practically do not change within the errorbars.

4.3. Chemical abundances

We calculated the elemental chemical abundances of our targets following the same procedure adopted in some of our previous works related to the SPA project (see, e.g., Frasca et al. 2019; Alonso-Santiago et al. 2021), which is based on the spectral synthesis technique (Catanzaro et al. 2011, 2013). In a first step we computed 1D local thermodynamic equilibrium (LTE) atmospheric models with the ATLAS9 code (Kurucz 1993a,b), adopting the ROTFIT atmospheric parameters (Sect. 4.2). Then, we generated the corresponding synthetic spectra using SYNTHE as the radiative transfer code (Kurucz & Avrett 1981). We compared the observed spectra with the synthetic ones (adequately broadened taking into account both the instrumental profile and the rotational one) in 39 spectral segments of 50 \AA each between 4400 and 6800 \AA . Finally, by minimising the χ^2 of their differences, the chemical abundances are found. In this way, for those stars with $T_{\text{eff}} < 7500 \text{ K}$, nine in total, we investigated 21 elements with atomic number up to 56 namely, C, Na, Mg, Al, Si, S, Ca, Sc, Ti, V, Cr, Mn, Fe, Co, Ni, Cu, Zn, Sr, Y, Zr, and Ba. Individual abundances are listed according to the standard notation $A(X) = \log[n(X)/n(H)] + 12$ in Table A.3 and an example of the spectral synthesis is shown in Fig. A.5. The cluster average composition, relative to solar abundances by Grevesse et al. (2007), is also reported in Table 4. For each element, it has been calculated by taking the weighted average of the values for each star, using the individual errors as weights. The uncertainties express, in terms of standard deviation, the dispersion of stellar abundances around the cluster value.

We find that the cluster, on average, exhibits a solar-like composition, with a metallicity of $[\text{Fe}/\text{H}] = +0.04 \pm 0.08 \text{ dex}$. Only Na shows a significant subsolar abundance ($[\text{Na}/\text{Fe}] = -0.25 \pm 0.13$). For the α -elements the weighted-mean ratio is $[\alpha/\text{Fe}] = +0.12 \pm 0.10 \text{ dex}$, with S being overabundant with respect to the other elements ($[\text{S}/\text{Fe}] = +0.30 \pm 0.12$). The Fe-peak elements show a solar ratio, $[\text{X}/\text{Fe}] = +0.05 \pm 0.10 \text{ dex}$, while the neutron-capture ones, especially Ba, have a supersolar value, $[\text{s}/\text{Fe}] = +0.28 \pm 0.10 \text{ dex}$. As expected, a homogeneous chemical composition is observed among the cluster members, with the only exception of star 3061, which in general displays lower abundances (i.e. Fe and Ti, see Fig. 4). On the contrary, star 3004, which was discarded as a member (see Sect. 3), has a chemical composition compatible with that of the cluster.

5. SED fitting and reddening

In order to evaluate how our observations are affected from interstellar extinction (A_V), we resorted to the spectral energy distribution (SED) fitting tool, as previously done in other works (Frasca et al. 2019; Alonso-Santiago et al. 2021). For each of our targets we fitted the corresponding SED with BT-Settl synthetic spectra (Allard 2014). To build the SED, on the one hand we made use of publicly available optical and near-infrared photo-

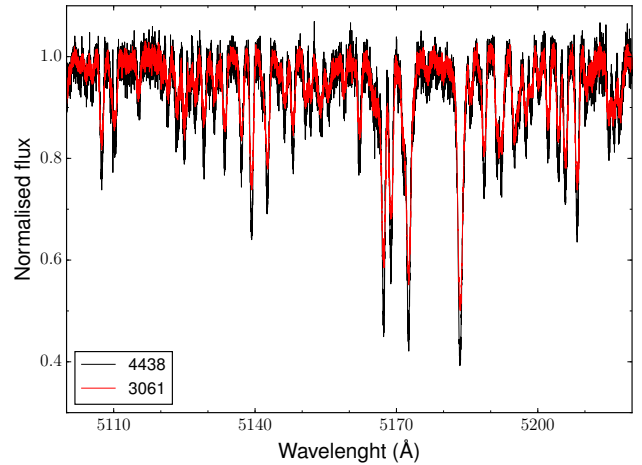


Fig. 4. Comparison of the spectra of two cluster stars with similar stellar parameters in the region of Mg Ib triplet. Star 4438 shows a chemical composition similar to that of other cluster members while star 3061 exhibits a somewhat lower value, which is also suggested by its shallower lines.

metric data. Specifically, we used the $BVg'r'i'$ (from the APASS catalogue, Henden et al. 2016), JHK_S (2MASS, Skrutskie et al. 2006) and $W_1W_2W_3W_4$ bands (WISE, Cutri & et al. 2012). On the other hand, we adopted the atmospheric parameters (T_{eff} and $\log g$) derived in Sect. 4.2 as well as the (corrected) *Gaia*-DR3 parallax. The stellar radius (R) and the A_V were set as free parameters. Their best values were obtained by χ^2 minimisation. The errors on A_V and R are found by the minimisation procedure considering the 1σ confidence level of the χ^2 map, but we also took the error on the T_{eff} into account. An example of this fitting is shown in Fig. 5.

The results of the SED fitting are reported in Table 5. Among the members analysed the A_V ranges from 0.00 to 0.38 mag, with an average of $A_V = 0.06 \pm 0.10$, where the error is the standard deviation. For most stars the reddening is on the cluster average with only star 7140 showing a slightly different value, 0.38 mag, the largest in the sample. If we recalculate the average without taking this star into account we obtain $A_V = 0.04 \pm 0.05 \text{ mag}$, where the dispersion has decreased. This result indicates that extinction is negligible in the cluster field, in good agreement with the literature (Cantat-Gaudin et al. 2018, $A_V = 0.0 \text{ mag}$).

6. Colour-magnitude diagrams

To investigate the cluster age, we resorted to the isochrone-fitting method. In a first step we used archival photometry to plot the colour-magnitude diagram (CMD) of the cluster, which is a snapshot of its evolutionary stage. Then, we looked for the age-dependent model, the isochrone, that best reproduced the position of the cluster members on the CMD. To compute the different isochrones we took advantage of the results previously obtained from spectroscopy, that is metallicity (Sect. 4.3) and reddening (Sect. 5).

We used three different photometric systems (Johnson, 2MASS and *Gaia*) to construct the following diagrams: $M_V/(B-V)_0$, $M_{K_S}/(J-K_S)_0$ and $M_G/(G_{BP}-G_{RP})_0$. In each of the diagrams the number of plotted members is different (111, 252 and 265, respectively) since photometric data is not always available for all of them. To convert apparent to absolute magnitudes we used

Table 3. Stellar parameters derived for the stars observed in this work.

Star	T_{eff} (K)	$\log g$	[Fe/H]	Sp T	$v \sin i$ (km s ⁻¹)	RV (km s ⁻¹)
Members						
0305	5783±73	4.40±0.13	0.03±0.13	G2 V	3.8±1.2	-5.34±0.06
2451	10000±400	4.00±0.20	0.00*	A0 V	110.0±20.0	-3.15±0.70
3061	6314±147	3.88±0.12	-0.40±0.10	F8 V	37.7±1.7	-6.07±0.69
3288	5772±65	4.29±0.10	0.13±0.12	G5 IV-V	4.3±0.7	-5.77±0.07
3311	7400±160	4.20±0.20	0.06±0.11	A9 V	42.5±1.3	-6.14±0.23
4265	10100±400	4.00±0.20	0.00*	A0 V	52.1±2.3	-5.28±0.64
4322	5782±69	4.44±0.11	0.03±0.12	G2 V	7.5±0.7	-5.87±0.07
4438	6233±138	3.89±0.12	0.07±0.17	F7 IV	26.4±1.5	-6.63±0.47
4673	8700±500	4.00±0.20	0.00*	A3 V	128.4±8.0	-3.16±0.50
5045	9100±200	3.50±0.20	0.00*	A1 V	51.4±2.3	-3.31±0.46
5609	7150±150	4.30±0.20	-0.12±0.12	F0 V	142.4±11.8	-10.94±2.02
5729	8000±400	4.00±0.20	0.00*	A6 V	190.0±20.0	-5.99±0.49
6791	8000±400	4.00±0.20	0.00*	A6 V	122.6±8.2	-5.68±0.60
7140	9900±400	4.00±0.20	0.00*	A0 V	75.0±10.0	-4.10±0.75
ucac	5783±78	4.41±0.12	0.06±0.10	G1 V	6.1±1.2	-4.78±0.08
Non-members						
3004	6921±270	4.22±0.15	0.08±0.14	F2 V	25.7±2.5	-5.73±0.48
4294	10200±350	4.00±0.20	0.00*	B9.5 V	110.0±20.0	-2.10±0.80

* Solar metallicity has been adopted for the hottest stars of our sample, as explained in the text.

Table 4. Average chemical composition of M 39, relative to solar abundances by Grevesse et al. (2007), derived in this work.

X	[X/H]	X	[X/H]
C	+0.10 ± 0.15	Mn	+0.10 ± 0.10
Na	-0.21 ± 0.11	Fe	+0.04 ± 0.08
Mg	+0.12 ± 0.07	Co	+0.05 ± 0.06
Al	+0.18 ± 0.06	Ni	+0.00 ± 0.05
Si	+0.07 ± 0.09	Cu	+0.15 ± 0.07
S	+0.34 ± 0.09	Zn	-0.03 ± 0.19
Ca	+0.19 ± 0.07	Sr	+0.32 ± 0.08
Sc	+0.11 ± 0.07	Y	+0.27 ± 0.02
Ti	+0.11 ± 0.15	Zr	+0.29 ± 0.08
V	+0.22 ± 0.05	Ba	+0.41 ± 0.04
Cr	+0.15 ± 0.04		

the individual distance of each source. We calculated it as the inversion of the parallax, once it was corrected as explained above (Sect. 3).

In the two first CMDs the reddening was corrected individually for those stars observed in this work with the value previously derived, while for the remaining stars the mean cluster value was applied. In the *Gaia* CMD we made use of the A_G and $E(G_{BP} - G_{RP})$ published in the DR2. When comparing all the three CMDs we immediately realised that the brightest stars in the upper MS behaved anomalously in the $M_V/(B - V)_0$ diagram compared to the other two. This is due to the fact that these stars (with $V \approx 7$ mag) are likely saturated in the APASS photometry. In order to fix this issue we resorted to the ASCC2.5 catalogue (Kharchenko & Roeser 2009), from which we took V and $(B - V)$ for six stars brighter than $V=8$ after scaling both photometric datasets³. The distribution of these stars on the CMD improved

³ We selected 25 members with good photometry in both catalogues in the range $7.5 \leq V \leq 10.5$, finding average differences (ASCC2.5 minus APASS) of $\Delta V=0.009$ and $\Delta(B - V)=-0.019$.

Table 5. Results of the SED fitting.

Star	A_V (mag)	R (R_\odot)	L (L_\odot)
Members			
0305	0.00±0.05	0.92±0.01	0.8±0.1
2451	0.11±0.07	3.56±0.07	113.9±18.2
3061	0.00±0.03	1.24±0.01	2.2±0.2
3288	0.04±0.07	0.80±0.01	0.6±0.1
3311	0.00±0.08	1.47±0.01	5.9±0.5
4265	0.09±0.07	2.49±0.04	55.6±8.8
4322	0.03±0.07	0.93±0.01	0.9±0.1
4438	0.00±0.01	1.24±0.07	2.1±0.3
4673	0.00±0.03	1.89±0.11	18.4±4.7
5045	0.16±0.12	5.10±0.13	160.8±14.4
5609	0.09±0.10	1.58±0.02	6.0±0.5
5729	0.00±0.01	1.87±0.13	13.0±3.1
6791	0.01±0.16	1.64±0.04	9.9±2.0
7140	0.38±0.11	1.62±0.04	22.6±3.6
ucac	0.06±0.10	0.87±0.01	0.8±0.1
Non-members			
3004	0.00±0.03	1.49±0.03	4.6±0.7
4294	0.55±0.13	6.10±0.06	335.0±46.7

considerably after this correction, so that we decided to use these magnitudes (listed in Table A.2 and displayed in Fig. 6) in this work.

Once the dereddened CMDs were built, we overplotted on them a set of isochrones of different ages to find the one that best reproduced the distribution of the cluster members and, thus, find the likely age for the cluster. We used PARSEC isochrones (Marigo et al. 2017) computed at the metallicity found in this work ([Fe/H]=0.04) in a wide range of ages ($\log \tau=8.2-8.9$, which corresponds to ages from 160 to 780 Ma). We carefully

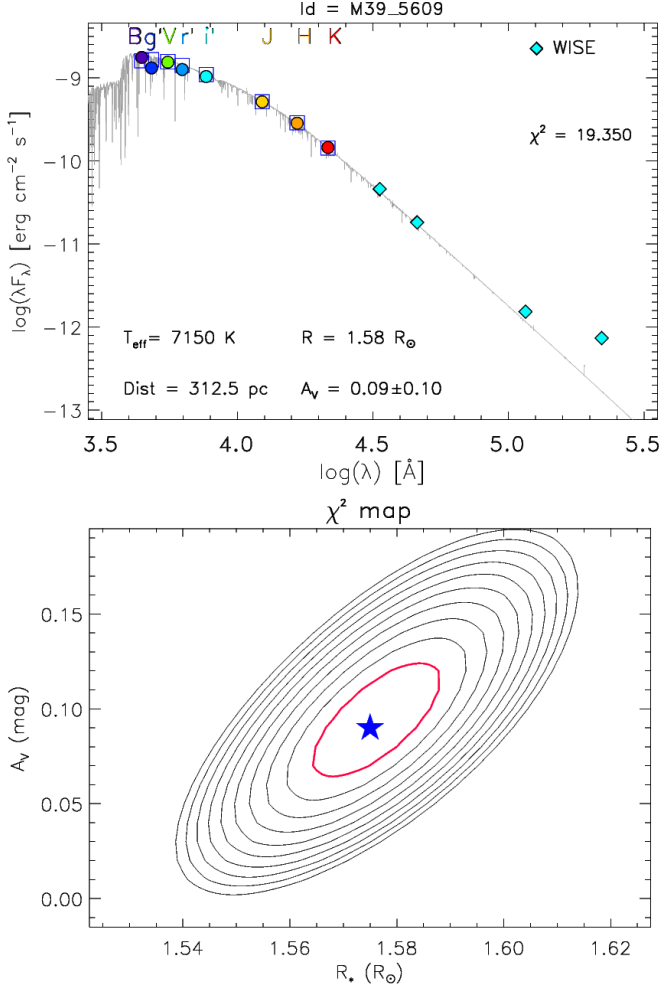


Fig. 5. Top: SED fitting of the star 5609. Bottom: χ^2 -contour map of the fitting. The red line corresponds to the 1 σ confidence level

examined by eye how well the isochrones (in steps $\Delta \log \tau = 0.01$) fitted the CMDs. Since there are no giants we had to pay attention to the stars located at the upper part of the MS. We noted that the best-fitting isochrone is not exactly the same in all the diagrams, but perfectly compatible within the errors. From the optical CMD we find an age for the cluster of 460 ± 100 Ma, similar to that obtained from the infrared one, 400 ± 150 Ma. The errors represent the interval of isochrones that are capable of reproducing the CMD.

In the case of the *Gaia* CMD, it is worth highlighting the role that reddening plays. As previously commented, we started taking the *Gaia* data for the reddening and extinction. When available we used individual values, as we did in previous works. However, for the rest of members we estimated these two values by averaging those of the five nearest stars (using their distances as weights). Nevertheless, the average reddening that can be deduced for our members from the *Gaia* DR3 catalogue, namely $A_G = 0.30 \pm 0.23$ and $E(G_{BP} - G_{RP}) = 0.20 \pm 0.14$, is quite different from the one calculated by us and exhibits a greater dispersion. When adopting it, the age of cluster becomes ≈ 300 Ma, somewhat younger than the age derived from the other CMDs. If we instead redden the isochrone with the A_V derived in this work, the dispersion of the stars along the MS decreases and the isochrones fit better the CMD. In this way, the cluster turns out

Table 6. Radial and rotational velocities for the stars observed by Mermilliod et al. (2009) in common with this work (TW).

Star	Me09		TW	
	RV	$v \sin i$	RV	$v \sin i$
0305	-5.01 ± 0.27	6.3 ± 2.8	-5.34 ± 0.06	4.0 ± 0.9
3004	-6.91 ± 0.76	23.7 ± 2.5	-5.73 ± 0.48	25.7 ± 2.5
3061	-5.14 ± 0.90	40.0 ± 4.0	-6.07 ± 0.69	37.7 ± 1.7
3288	-5.76 ± 0.40	5.8 ± 2.1	-5.77 ± 0.07	4.3 ± 0.7
4322	-6.45 ± 0.22	4.9 ± 2.0	-5.87 ± 0.07	7.5 ± 0.7

to be of 420 ± 80 , a value comprised between those derived from the other two CMDs. This difference between our extinction and that derived from *Gaia* data could be explained by the known fact that *Gaia*-DR3 tends to overestimate the extinction in areas of the sky where its value is very low (Andrae et al. 2023; Babusiaux et al. 2023; Fouesneau et al. 2023).

Finally, the definitive age of the cluster is obtained by averaging the estimates derived from each CMD, using the individual uncertainties as weights. The resulting value is 430 ± 110 Ma, which corresponds to a MSTO mass of around $2.8 M_\odot$. As error we took the mean of each uncertainty. The CMDs, along with the best-fitting isochrones and their uncertainties, are shown in Fig. 6. This result agrees very well with that reported in Cantat-Gaudin et al. (2020).

7. Discussion

7.1. Radial and rotational velocities

M39 was one of the nearby clusters containing FK dwarfs observed by Mermilliod et al. (2009). They derived radial and rotational velocities for 24 stars in the cluster field, out of which six stars are also included in our sample. Star 3423 is one of the targets in common in both studies, but in our spectrum it appears as an SB2, with two strongly blended peaks in the CCF, whose velocities are $RV_1 = -7.98 \pm 1.47$ km s⁻¹ and $RV_2 = -2.09 \pm 0.19$ km s⁻¹, with the former having a much larger width compared to the latter (see Fig. A.3). Mermilliod et al. (2009) did report no binary signature for this star. This has likely arisen from having observed the system near to a conjunction. In fact, they measured an $RV = -5.90 \pm 0.73$ km s⁻¹, that, if considered as the RV of centre of mass of the system, is in good agreement with the mean of the RVs of the two components in our spectrum. For the remaining five objects both sets of measurements, RV and $v \sin i$, are in excellent agreement in both papers (see Table 6). In addition, the mean RV of the cluster calculated by Mermilliod et al. (2009) from 17 members, $RV = -5.26 \pm 0.30$ km s⁻¹, is fully compatible with that derived in this work.

7.2. Chromospheric emission and lithium abundance

A way of estimate the age of the stars that are forming the cluster, independent of the isochrone-fitting method, is the evaluation of the level of magnetic activity (e.g., the emission in the cores of lines formed in the chromosphere) and the abundance of Li present in their atmospheres. This is valid for stars cooler than ≈ 6500 K and ages between a few ten and a few hundred Ma (see Jeffries 2014; Frasca et al. 2018, and references therein).

In order to perform this task we applied the subtraction technique. It consists in subtracting the spectrum of a pertinent template from that of the target to measure the excess emission in the chromospheric lines and the equivalent width of the Li I $\lambda 6708$ Å

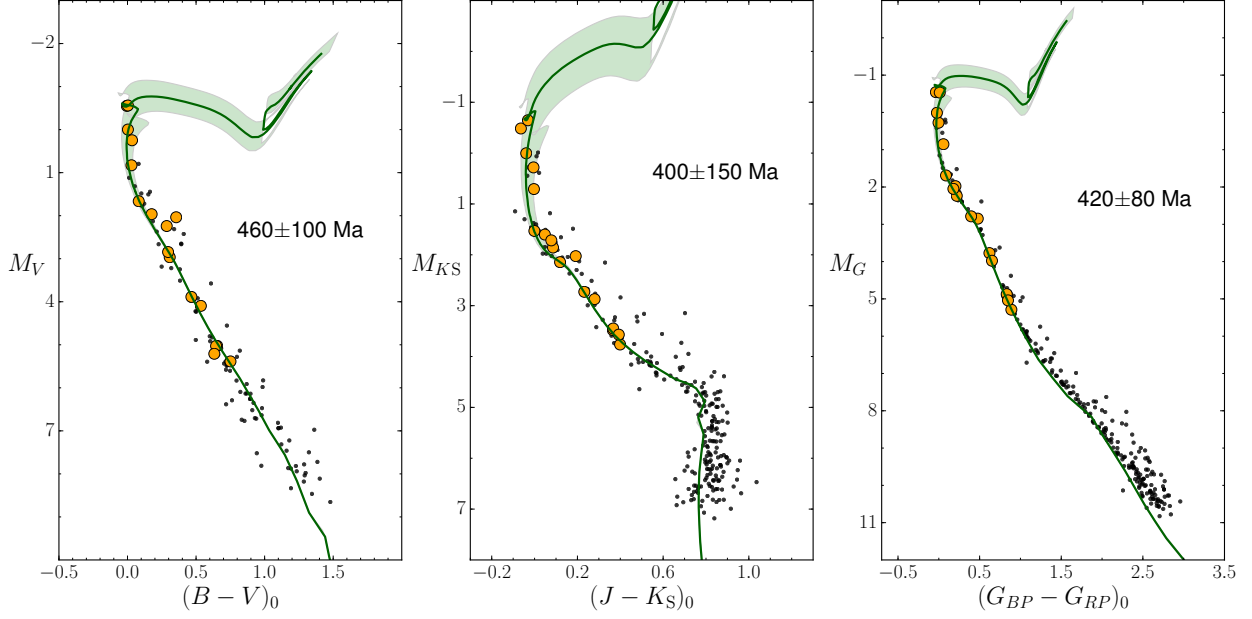


Fig. 6. Colour-magnitude diagrams for M39 in three different photometric systems. *Left:* $M_V/(B - V)_0$, photometric data from the APASS catalogue. *Centre:* $M_{KS}/(J - K_S)_0$ (2MASS). *Right:* $M_G/(G_{BP} - G_{RP})_0$ (Gaia-DR3). The small black points are the members selected in this work and the orange circles mark those ones observed spectroscopically. The green lines and the shaded area are the best-fitting isochrones with the associated uncertainties. The age derived from each CMD is also shown.

absorption line (EW_{Li}). An example of this procedure is shown in Fig. 9. As templates we used the spectra of non-active and lithium-poor stars, Doppler-shifted and rotationally broadened by ROTFIT. As diagnostics of activity we used the Balmer $H\alpha$ line and the $Ca II$ H&K lines. The latter lines are located in the bluest part of the spectra where the S/N is very low, but degrading the spectra resolution from 115,000 to that of ELODIE ($R = 42,000$) allowed us to improve the S/N and apply the spectral subtraction. For the $Ca II$ lines, the photospheric templates are made with synthetic BT-Settl spectra (Allard 2014) as we did in Frasca et al. (2023a), because they are best suited to reproduce the photospheric spectrum without any chromospheric contribution compared to the low-activity real stars. Indeed, for the latter a small line emission or filling is very often present in the cores of the $Ca II$ H&K lines.

From the atmospheric parameters and the EW_{Li} we estimated the lithium abundance, $A(Li)$, by interpolating the curves of growth of Soderblom et al. (1993), calculated in the T_{eff} range 4000–6500 K. The lithium abundance is reported in Table 7 and is plotted versus T_{eff} in Fig. 7. The upper envelopes of four young clusters, namely the Hyades (650 Ma), NGC 6475 (300 Ma), the Pleiades (125 Ma), and IC 2602 (30 Ma), adapted from Sestito & Randich (2005), are overlaid with different colors. All the solar-type members display values of $A(Li)$ compatible with an age greater than 300 Ma.

To estimate the age of the cluster from the content of photospheric lithium, we also used the EAGLES code (Jeffries et al. 2023), as we did in Frasca et al. (2023b). This code, based on an empirical model, is very suitable for a cluster since it determines the age probability distribution for the ensemble from the T_{eff} and EW_{Li} of its members. In the present case, we obtained an age for M 39 of $\tau = 570^{+270}_{-190}$ Ma (see Fig. 8). This value is greater than the one obtained with the fitting-isochrone method, but compatible within the errors. In any case, the age uncertainty is larger

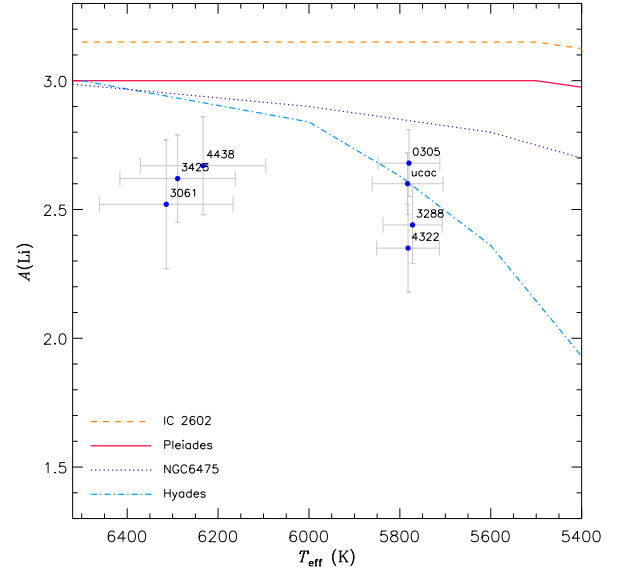


Fig. 7. Lithium abundance as a function of T_{eff} for the solar-type members ($T_{eff} < 6500$ K). The upper envelopes of $A(Li)$ for four young clusters adapted from Sestito & Randich (2005) are overlaid.

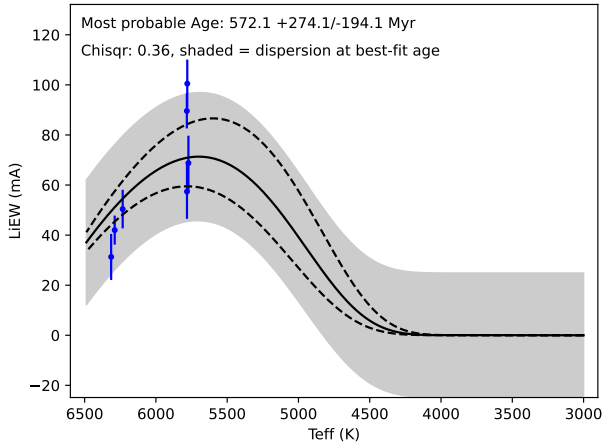
than one could expect, mainly due to the data scatter and the poor T_{eff} distribution of the targets, and it does not allow us to provide us with a good age constraint.

The excess $H\alpha$ equivalent width, $EW_{H\alpha}^{em}$, has been obtained by integrating the $H\alpha$ emission profile, resulting by the subtraction of the photospheric template, which is highlighted by the green hatched area in the difference spectra of Fig. 9. Similarly, the difference between the observed and template spectrum in

Table 7. Li I λ 6708 Å equivalent width and abundance for the cool stars observed in this work.

Star	T_{eff} (K)	EW_{Li} (mÅ)	$A(\text{Li})$
0305	5783 ± 73	100 ± 10	2.68 ± 0.13
3004	6921 ± 270	29 ± 9	$2.63 \pm 0.14^*$
3061	6314 ± 147	31 ± 9	2.52 ± 0.25
3288	5772 ± 65	69 ± 11	2.44 ± 0.15
3311	7088 ± 160	28 ± 6	$2.60 \pm 0.11^*$
4322	5782 ± 69	57 ± 11	2.35 ± 0.17
4438	6233 ± 138	50 ± 8	2.67 ± 0.19
5609	7029 ± 167	4 ± 4	$< 2.03^*$
ucac	5783 ± 78	90 ± 7	2.60 ± 0.12

* $T_{\text{eff}} > 6500$ K. $A(\text{Li})$ extrapolated from the Soderblom et al. (1993) tables.

**Fig. 8.** Fit to the Li depletion pattern of the cool members of M 39 made with the EAGLES code.

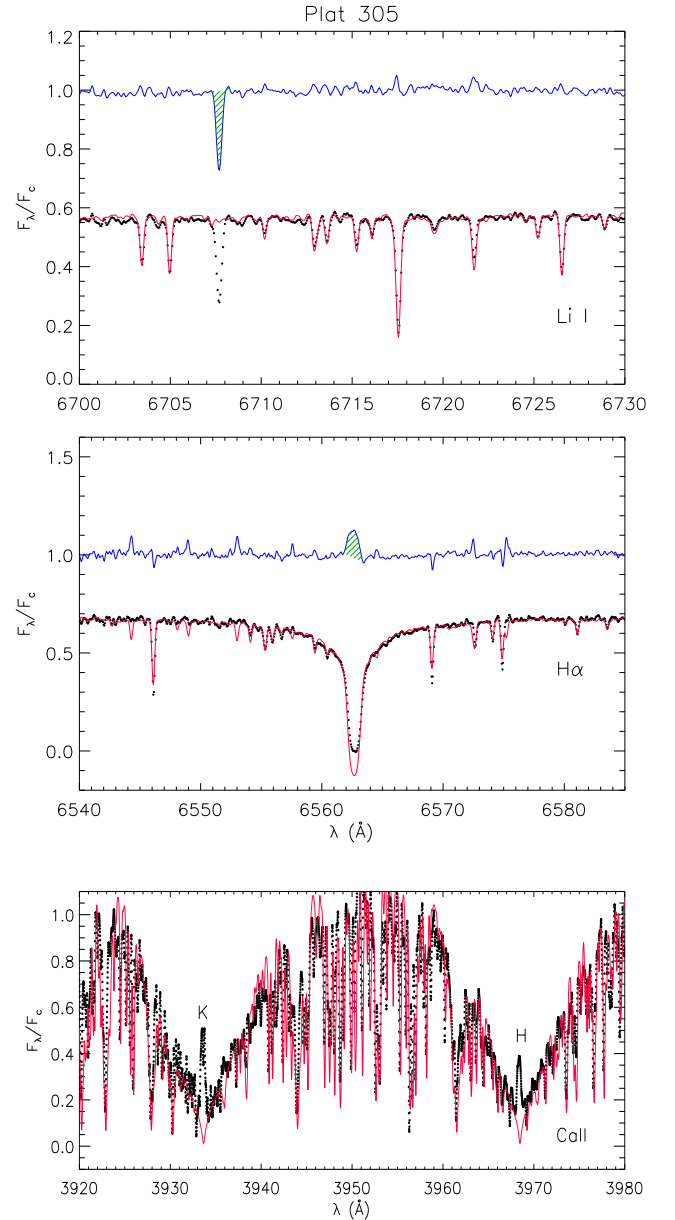
the Ca II region leaves emission excesses in the cores of the H and K lines, whose integration provide the equivalent widths, $EW_{\text{CaII-H}}$ and $EW_{\text{CaII-K}}$. More effective indicators of chromospheric activity are the chromospheric line fluxes at the stellar surface, F_{line} , and the luminosity ratios, $R'_{\text{line}} = F_{\text{line}}/F_{\text{bol}}$, where $F_{\text{bol}} = \sigma T_{\text{eff}}^4$ is the bolometric flux. For the Ca II K, the line flux can be calculated as

$$F_{\text{CaII-K}} = F_{3933} EW_{\text{CaII-K}}, \quad (1)$$

where F_{3933} is the flux at the continuum at the center of the Ca II-K line per unit stellar surface area, which is evaluated from the BT-Settl spectra (Allard 2014) at the stellar temperature and surface gravity of the target. The flux error include the error in the equivalent width and the uncertainty in the continuum flux at the line center, which is estimated propagating the errors of T_{eff} and $\log g$.

We computed surface fluxes for the other chromospheric diagnostics in the same way as for the Ca II-K line. The EWs, fluxes, and luminosity ratios are reported in Table 8 for the solar-type stars ($T_{\text{eff}} < 6500$ K).

We used the age–activity relation proposed by Mamajek & Hillenbrand (2008) to estimate the age of M 39. From their Eq. 3

**Fig. 9.** Spectral subtraction for the star 0305 in the Li I λ 6708 Å, H α , and Ca II H&K lines (from top to bottom).

and our values of R'_{HK} , which are reported in Table 8, we estimate an age of 250 ± 150 Ma, which is smaller than the values derived from both the CMD and lithium isochrones, but marginally compatible with them if we consider the large age errors.

7.3. Galactic metallicity gradient

Open clusters are known to be among the best tracers of the radial distribution of metallicity in the Galaxy, the so-called Galactic gradient. With the aim of evaluating how the metallicity obtained in this work for M 39 compares with this gradient, we searched for a sample of homogeneously analysed clusters from the literature. We gathered the metallicity derived with high-resolution spectroscopy within the framework of the *Gaia*-ESO (Randich et al. 2022) and the OCCAM (APOGEE-DR17, Myers et al. 2022) surveys. Additionally, clusters targeted in the SPA project (Frasca et al. 2019; D’Orazi et al. 2020; Casali et al.

Table 8. $H\alpha$ and Ca II H & K equivalent widths and fluxes.

Star	$EW_{H\alpha}$ (mÅ)	$F_{H\alpha}$ ($10^5 \text{ erg cm}^{-2} \text{ s}^{-1}$)	$R'_{H\alpha}$	$EW_{\text{CaII-K}}$ (mÅ)	$EW_{\text{CaII-H}}$ (mÅ)	$F_{\text{CaII-K}}$ ($10^5 \text{ erg cm}^{-2} \text{ s}^{-1}$)	$F_{\text{CaII-H}}$ ($10^5 \text{ erg cm}^{-2} \text{ s}^{-1}$)	R'_{HK}
0305	126±21	9.2±1.6	-4.84	262±88	213±83	15.0±5.3	12.2±4.9	-4.37
3061	59±15	5.9±1.6	-5.18	157±40	110±44	18.7±5.9	13.2±5.8	-4.45
3288	111±22	8.2±1.7	-4.88	410±226	194±226	23.1±12.9	11.0±12.8	-4.27
4322	200±34	14.9±2.6	-4.63	331±130	225±167	18.9±7.6	12.8±9.6	-4.30
4438	96±14	9.4±1.6	-4.96	207±60	181±81	22.4±7.5	19.6±9.4	-4.31
ucac	146±22	10.7±1.7	-4.77	256±101	230±115	14.7±6.0	13.1±6.7	-4.37

2020; Zhang et al. 2021; Alonso-Santiago et al. 2021) and some other young open clusters studied by our group complete the sample (Alonso-Santiago et al. 2017, 2018, 2019, 2020). In total we collected a sample containing nearly two hundreds clusters at Galactocentric distances, R_{GC} , up to 16 kpc. The position of M 39 on this gradient is shown in Fig. 10. The metallicity, as the abundance of iron, was referenced to $A(\text{Fe})=7.45$ (Grevesse et al. 2007). Galactocentric distances were taken from Cantat-Gaudin et al. (2020), who calculated them from *Gaia*-DR2 astrometry and taking as a reference a solar value of $R_{\odot}=8.34$ kpc. As can be seen, the metallicity derived in this work is compatible with that expected for the cluster location.

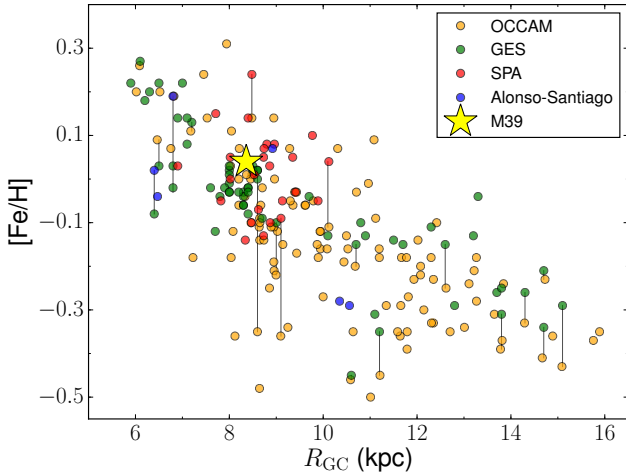


Fig. 10. Radial metallicity gradient from open clusters studied in the framework of the *Gaia*-ESO and OCCAM Surveys, the SPA project and some other clusters analysed by Alonso-Santiago. Black lines link results for the same cluster provided by different authors. The star represents the metallicity found in this work for M 39.

7.4. Chemical composition and Galactic trends

As commented before (see Sect. 1) this work provides for the first time chemical abundances for M 39. Thus, due to the lack of specific literature with which to compare our results, we resorted to the chemical trends displayed by Galactic open clusters. We used the same sample previously employed when discussing about the Galactic gradient but in this case, chemical abundances for the GES (iDR6) and SPA clusters are taken from Magrini et al. (2023) and Zhang et al. (2022) respectively, since Randich et al. (2022) and Zhang et al. (2021) only provided metallicity values. We compared the chemical composition of

M 39 with that of the other open clusters collected in our sample. Figure 11 shows the ratios $[X/\text{Fe}]$ versus $[\text{Fe}/\text{H}]$ for 16 chemical elements (scaled to the solar abundances listed in Grevesse et al. 2007). The abundances of M 39 are in a great agreement with the trends outlined by so many other open clusters collected in our sample and, therefore, we conclude that its chemical composition is fully compatible with that of the Galactic thin disc. All the elements are on the trends or slightly above them. Only Na, the sole element in sample with a clearly subsolar abundance, and S are located further away from the bulk of the rest of the clusters, but always in a compatible place.

8. Summary and conclusions

We conducted this research with the idea of adding one more tile to the mosaic of Galactic Archaeology that will help us improve our knowledge about the formation and evolution of the Milky Way. We focused on M 39, a nearby young open cluster little-studied in recent years, whose chemical composition was so far unknown. We performed high-resolution spectroscopy with the HARPS-N and FIES spectrographs for 20 likely cluster members that were supplemented with archival photometry and *Gaia*-DR3 data.

According to the literature, M 39 is formed only by MS stars. In order to find any giant that belongs to the cluster we searched for new members. We recalculated the members identified by Cantat-Gaudin et al. (2018) taking advantage of the latest *Gaia*-DR3 astrometry. We expand their list, finding 260 likely members within a radius of $250''$ around the nominal cluster centre. Among them, no evolved stars have been found. By examining the spatial distribution of the members we infer a distance to the cluster of 300 pc.

We find three SB2s in our sample. For the remaining stars, we derived their radial and projected rotational velocities and estimated the extinction and their atmospheric parameters. Additionally, for the coolest stars, nine in total, we carried out the chemical analysis, providing abundances for 21 elements. We do not find a significant reddening along the cluster field and estimate a mean RV of $-5.5 \pm 0.5 \text{ km s}^{-1}$. By fitting isochrones on three different CMDs we find an age for the cluster of $430 \pm 110 \text{ Ma}$, which is consistent with the content of Li and chromospheric activity found among the members.

M 39 shows a solar-like metallicity, $[\text{Fe}/\text{H}] = +0.04 \pm 0.08 \text{ dex}$, which is consistent with that expected for its Galactocentric distance. We performed the first detailed study of the chemical composition of the cluster to date. We determined the abundances of C, odd-Z elements (Na, Al), α -elements (Mg, Si, S, Ca, Ti), Fe-peak elements (Sc, V, Cr, Mn, Co, Ni, Cu, Zn) and s-elements (Sr, Y, Zr, Ba). The cluster stars have a chemical composition similar to that of the Sun. Only Na shows a lower abundance, while S and the heaviest elements, specially

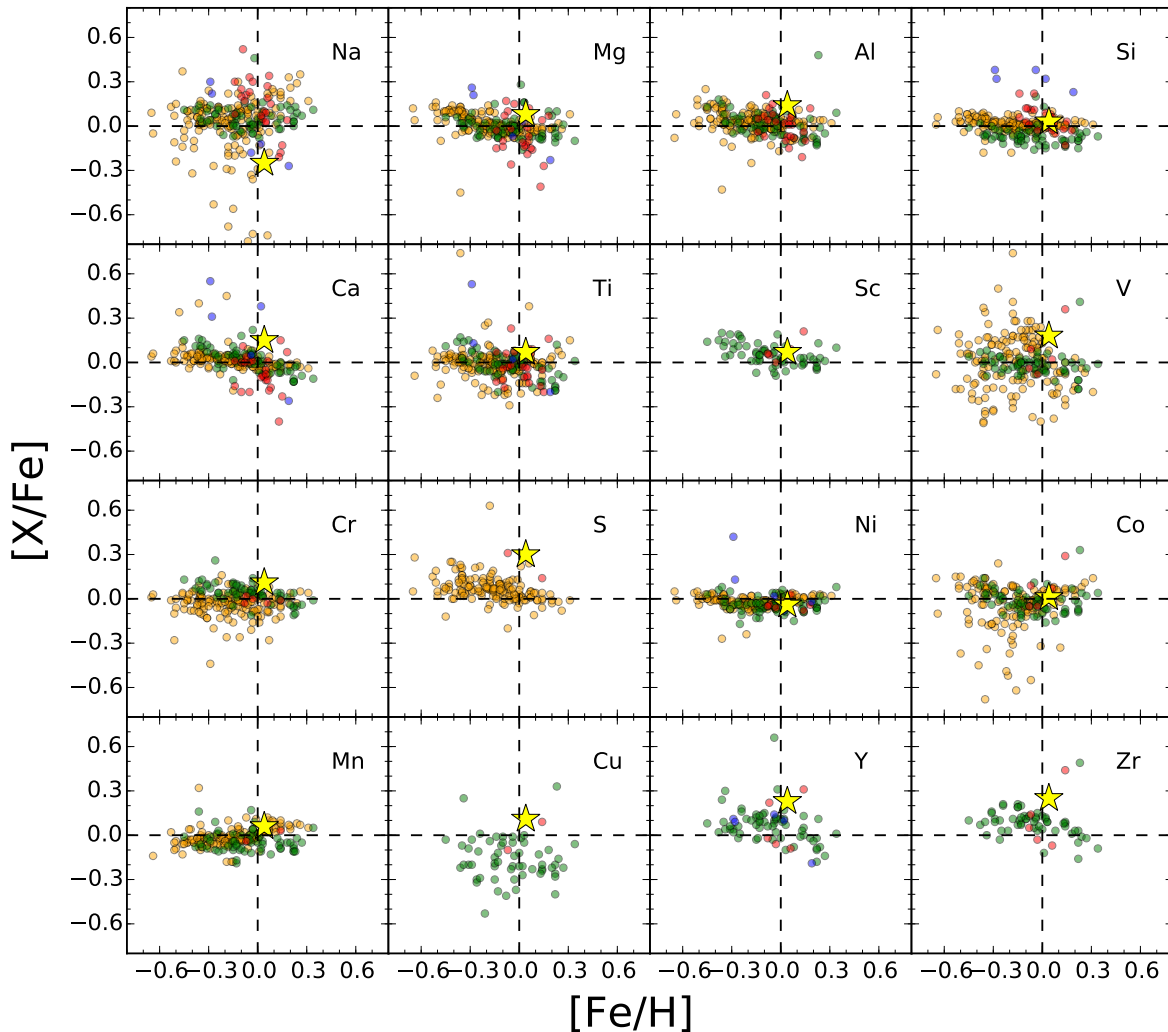


Fig. 11. Abundance ratios $[X/Fe]$ vs. $[Fe/H]$. Symbols and colours are the same as in Fig. 10. The dashed lines show the solar value.

Ba, display higher values. Its ratios $[X/Fe]$ are on the Galactic trends displayed by the large sample of open clusters studied in surveys such as the *Gaia*-ESO, OCCAM or SPA. The cluster shows solar-like mean ratios for α ($[\alpha/Fe]=+0.12\pm0.10$ dex) and Fe-peak elements ($[X/Fe]=+0.05\pm0.10$ dex), while for the neutron-capture elements the ratio is slightly overabundant ($[s/Fe]=+0.28\pm0.10$ dex). Finally, we conclude our research by claiming that the chemical composition of M 39 is fully compatible with that of the Galactic thin disc.

Acknowledgements

Based on observations made with the Italian *Telescopio Nazionale Galileo* (TNG) operated on the island of La Palma by the Fundación Galileo Galilei of the INAF (*Istituto Nazionale di Astrofisica*) at the *Observatorio del Roque de los Muchachos*.

This research is also partially based on observations made with the Nordic Optical Telescope, owned in collaboration by the University of Turku and Aarhus University, and operated jointly by Aarhus University, the University of Turku and the University of Oslo, representing Denmark, Finland and Norway, the Univer-

sity of Iceland and Stockholm University at the Observatorio del Roque de los Muchachos, La Palma, Spain, of the Instituto de Astrofísica de Canarias.

The research leading to these results has received funding from the European Union Seventh Framework Programme (F7/2007-2013) under grant agreement No. 312430 (OPTICON).

References

- Abt, H. A. & Levato, H. 1976, *PASP*, 88, 222
- Abt, H. A. & Sanders, W. L. 1973, *ApJ*, 186, 177
- Allard, F. 2014, in *Exploring the Formation and Evolution of Planetary Systems*, ed. M. Booth, B. C. Matthews, & J. R. Graham, Vol. 299, 271–272
- Alonso-Santiago, J., Frasca, A., Catanzaro, G., et al. 2021, *A&A*, 656, A149
- Alonso-Santiago, J., Marco, A., Negueruela, I., et al. 2018, *A&A*, 616, A124
- Alonso-Santiago, J., Negueruela, I., Marco, A., Tabernero, H. M., & Castro, N. 2020, *A&A*, 644, A136
- Alonso-Santiago, J., Negueruela, I., Marco, A., et al. 2017, *MNRAS*, 469, 1330
- Alonso-Santiago, J., Negueruela, I., Marco, A., et al. 2019, *A&A*, 631, A124
- Andrae, R., Fouesneau, M., Sordo, R., et al. 2023, *A&A*, 674, A27
- Babusiaux, C., Fabricius, C., Khanna, S., et al. 2023, *A&A*, 674, A32
- Cantat-Gaudin, T., Anders, F., Castro-Ginard, A., et al. 2020, *A&A*, 640, A1
- Cantat-Gaudin, T., Jordi, C., Vallenari, A., et al. 2018, *A&A*, 618, A93

- Casali, G., Magrini, L., Frasca, A., et al. 2020, A&A, 643, A12
- Catanzaro, G., Ripepi, V., Bernabei, S., et al. 2011, MNRAS, 411, 1167
- Catanzaro, G., Ripepi, V., & Bruntt, H. 2013, MNRAS, 431, 3258
- Cosentino, R., Lovis, C., Pepe, F., et al. 2014, in Society of Photo-Optical Instrumentation Engineers (SPIE) Conference Series, Vol. 9147, Ground-based and Airborne Instrumentation for Astronomy V, ed. S. K. Ramsay, I. S. McLean, & H. Takami, 91478C
- Cutri, R. M. & et al. 2012, VizieR Online Data Catalog, II/311
- de Jong, R. S., Agertz, O., Berbel, A. A., et al. 2019, The Messenger, 175, 3
- De Silva, G. M., Freeman, K. C., Bland-Hawthorn, J., et al. 2015, MNRAS, 449, 2604
- D’Orazi, V., Oliva, E., Bragaglia, A., et al. 2020, A&A, 633, A38
- Ebbighausen, E. G. 1940, ApJ, 92, 434
- Eggen, O. J. 1951, ApJ, 113, 657
- Fouesneau, M., Frémat, Y., Andrae, R., et al. 2023, A&A, 674, A28
- Frasca, A., Alonso-Santiago, J., Catanzaro, G., & Bragaglia, A. 2023a, MNRAS, 522, 4894
- Frasca, A., Alonso-Santiago, J., Catanzaro, G., et al. 2019, A&A, 632, A16
- Frasca, A., Alonso-Santiago, J., Catanzaro, G., et al. 2023b, arXiv e-prints, arXiv:2307.14081
- Frasca, A., Biazzo, K., Lanzafame, A. C., et al. 2015, A&A, 575, A4
- Frasca, A., Freire Ferrero, R., Marilli, E., & Catalano, S. 2000, A&A, 364, 179
- Frasca, A., Guillout, P., Klutsch, A., et al. 2018, A&A, 612, A96
- Frasca, A., Guillout, P., Marilli, E., et al. 2006, A&A, 454, 301
- Gaia Collaboration, Vallenari, A., Brown, A. G. A., et al. 2022, arXiv e-prints, arXiv:2208.00211
- Gilmore, G., Randich, S., Worley, C. C., et al. 2022, A&A, 666, A120
- Grevesse, N., Asplund, M., & Sauval, A. J. 2007, Space Sci. Rev., 130, 105
- Henden, A. A., Templeton, M., Terrell, D., et al. 2016, VizieR Online Data Catalog, II/336
- Hunt, E. L. & Reffert, S. 2023, A&A, 673, A114
- Jeffries, R. D. 2014, in EAS Publications Series, Vol. 65, EAS Publications Series, ed. Y. Lebreton, D. Valls-Gabaud, & C. Charbonnel, 289–325
- Jeffries, R. D., Jackson, R. J., Wright, N. J., et al. 2023, MNRAS, 523, 802
- Jin, S., Trager, S. C., Dalton, G. B., et al. 2023, MNRAS, 667, A103
- Johnson, H. L. 1953, ApJ, 117, 353
- Kharchenko, N. V. & Roeser, S. 2009, VizieR Online Data Catalog, I/280B
- Kurucz, R. 1993a, ATLAS9 Stellar Atmosphere Programs and 2 km/s grid. Kurucz CD-ROM No. 13. Cambridge, 13
- Kurucz, R. L. 1993b, in Astronomical Society of the Pacific Conference Series, Vol. 44, IAU Colloq. 138: Peculiar versus Normal Phenomena in A-type and Related Stars, ed. M. M. Dworetzky, F. Castelli, & R. Faraggiana, 87
- Kurucz, R. L. & Avrett, E. H. 1981, SAO Special Report, 391
- Lindgren, L., Klioner, S. A., Hernández, J., et al. 2021, A&A, 649, A2
- Magrini, L., Viscasillas Vázquez, C., Spina, L., et al. 2023, A&A, 669, A119
- Majewski, S. R., Schiavon, R. P., Frinchaboy, P. M., et al. 2017, AJ, 154, 94
- Mamajek, E. E. & Hillenbrand, L. A. 2008, ApJ, 687, 1264
- Manteiga, M., Martinez-Roger, C., Morales, C., & Sabau, L. 1991, A&AS, 87, 419
- Marigo, P., Girardi, L., Bressan, A., et al. 2017, ApJ, 835, 77
- McNamara, B. J. & Sanders, W. L. 1977, A&AS, 30, 45
- Mermilliod, J. C., Mayor, M., & Udry, S. 2009, A&A, 498, 949
- Mohan, V. & Sagar, R. 1985, MNRAS, 213, 337
- Myers, N., Donor, J., Spoo, T., et al. 2022, AJ, 164, 85
- Platais, I. 1994, Bulletin d’Information du Centre de Données Stellaires, 44, 9
- Randich, S., Gilmore, G., Magrini, L., et al. 2022, A&A, 666, A121
- Sestito, P. & Randich, S. 2005, A&A, 442, 615
- Skrutskie, M. F., Cutri, R. M., Stiening, R., et al. 2006, AJ, 131, 1163
- Smiljanic, R., Korn, A. J., Bergemann, M., et al. 2014, A&A, 570, A122
- Soderblom, D. R., Jones, B. F., Balachandran, S., et al. 1993, AJ, 106, 1059
- Telting, J. H., Avila, G., Buchhave, L., et al. 2014, Astronomische Nachrichten, 335, 41
- Trumpler, R. J. 1928, PASP, 40, 265
- Weaver, H. F. 1953, ApJ, 117, 366
- Zhang, R., Lucatello, S., Bragaglia, A., et al. 2022, A&A, 667, A103
- Zhang, R., Lucatello, S., Bragaglia, A., et al. 2021, A&A, 654, A77

Appendix A: Additional materials

Table A.1. *Gaia* DR3 astrometric data and cluster membership, according to Platais (1994, P_{Pl}) and Cantat-Gaudin et al. (2018, P_{CG}), for all stars observed spectroscopically in this work (P_{TW}).

Star	<i>Gaia</i> -DR3 ID	RA (J2000)	DEC (J2000)	r ($'$)	P_{Pl}	P_{CG}	P_{TW}	ϖ (mas)	μ_{α^*} (mas a $^{-1}$)	μ_{δ} (mas a $^{-1}$)
Members										
0305	1978587946054581760	321.881658501	48.322025012	40.5	0.72	1.0	I	3.397	-7.488	-20.357
2451	1978555647899068544	322.578899973	48.390844737	15.1	0.97	0.9	I	3.367	-7.856	-19.652
3061	1978556644336044416	322.725446694	48.427086634	12.6	0.70	1.0	I	3.328	-7.537	-19.258
3288	1978699683923650688	322.782240751	48.644378692	24.2	0.77	1.0	I	3.432	-7.362	-20.054
3311	1978533142270627328	322.793918577	48.070524115	11.3	0.98	1.0	I	3.415	-7.497	-19.837
3781	1978652748518359808	322.926601311	48.584617826	20.3	0.97	1.0	I	3.324	-7.769	-19.771
3814	1978647762043764608	322.936042739	48.484353871	14.4	0.98	0.7	I	3.308	-8.004	-19.684
4265	1978656218831726848	323.061071758	48.639501413	24.5	0.97	1.0	I	3.291	-7.428	-19.568
4322	1978628593621993088	323.081133228	48.200479032	8.2	0.75	1.0	I	3.332	-7.743	-20.166
4438	1978740434565656320	323.114228026	49.181066745	56.7	0.78	1.0	I	3.340	-7.476	-19.720
4673	1978641856481498752	323.179813508	48.483167010	18.3	0.98	1.0	I	3.380	-7.614	-19.973
5045	1978443325910675712	323.292127855	48.303406860	16.5	0.98	...	I	3.325	-8.080	-19.576
5609	1978742908476235776	323.448921752	49.160993150	59.2	0.42	...	I	3.154	-7.165	-19.645
5729	1978743355145551104	323.486420337	49.196906735	61.7	0.70	1.0	I	3.308	-7.333	-19.552
6791	1978460471421230848	323.805577079	48.437269774	38.3	0.97	1.0	I	3.413	-7.613	-20.013
7140	1978404499404948096	323.948575257	48.108247352	43.2	0.96	1.0	I	3.363	-7.719	-19.540
ucac	1972328941741362944	320.502548884	46.489037684	143.3	...	1.0	I	3.234	-7.011	-19.731
Non-members										
3004	1978557640768446464	322.710204334	48.483127406	15.9	0.95	3.112	-7.358	-16.743
3423	1978652508006151296	322.825494272	48.623094206	22.7	0.72	3.050	-6.599	-22.305
4294	1978636290203508608	323.071129883	48.443836401	13.9	0.96	3.056	-5.833	-22.329

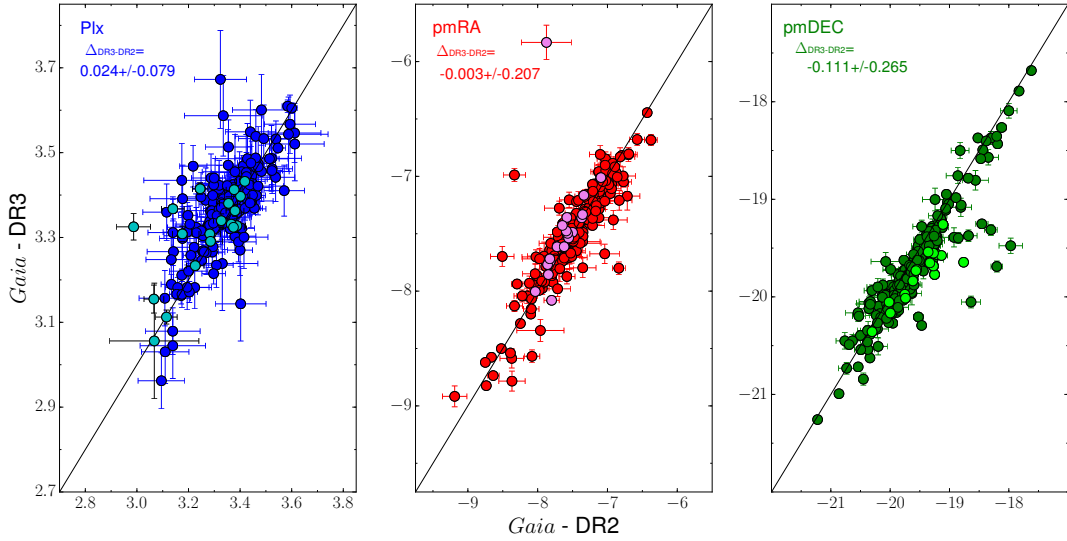
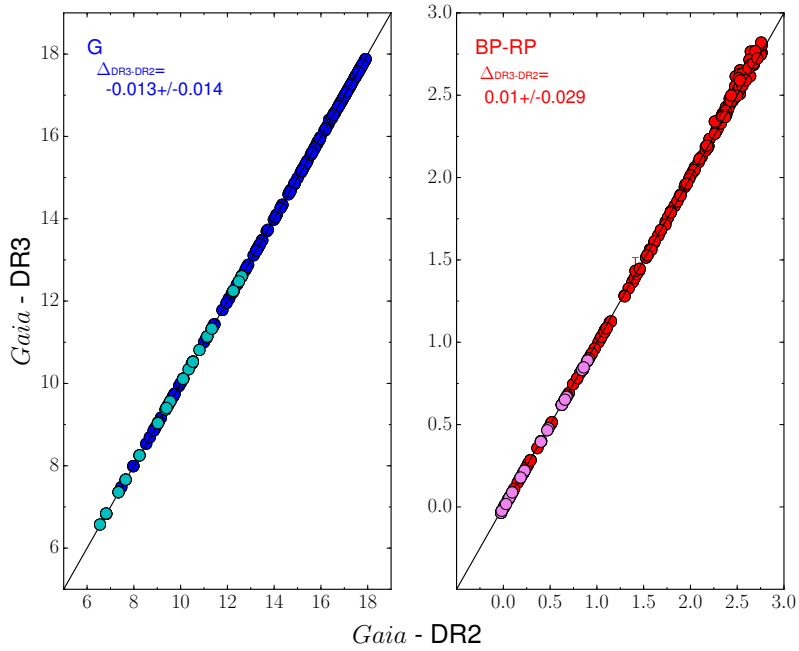
**Fig. A.1.** Astrometric data for the cluster members identified by Cantat-Gaudin et al. (2018) in *Gaia*-DR2 and *Gaia*-DR3. The lightest colour in each panel represents the stars observed in this work. For each parameter the mean difference (DR3-DR2) and its dispersion are indicated in the upper left part of the plots.

Table A.2. Photometry for stars observed spectroscopically in this work.

Star	V^a	$(B - V)^a$	J^b	H^b	K_S^b	G^c	$(G_{BP} - G_{RP})^c$	$E(G_{BP} - G_{RP})^c$	A_G^c
Members									
0305	12.359	0.654	11.178	10.854	10.813	12.231	0.836	0.000	0.002
2451	7.318*	0.121*	7.312	7.353	7.351	7.358	-0.023	0.041	0.076
3061	11.256	0.466	10.329	10.141	10.097	11.141	0.620	0.001	0.001
3288	12.698	0.751	11.474	11.144	11.075	12.602	0.889	0.023	0.042
3311	10.168	0.296	9.587	9.524	9.468	10.110	0.396	0.032	0.060
3781	6.961*	0.139*	6.826	6.846	6.890	6.831	-0.036	0.051	0.096
3814	7.630*	0.057*	7.663	7.608	7.668	7.663	-0.004	0.040	0.075
4265	8.228	0.029	8.104	8.084	8.107	8.252	0.056	0.132	0.247
4322	12.403	0.646	11.193	10.866	10.826	12.249	0.832	0.001	0.001
4438	11.447	0.535	10.503	10.288	10.223	11.329	0.651	0.003	0.005
4673	9.008	0.082	8.874	8.898	8.875	9.035	0.088	0.110	0.206
5045	6.691*	0.195*	6.697	6.778	6.728	6.840	0.012	0.048	0.091
5609	10.460	0.308	9.713	9.567	9.521	10.343	0.477	0.016	0.029
5729	9.356	0.176	9.041	8.997	8.993	9.369	0.204	0.032	0.060
6791	9.565	0.286	9.267	9.142	9.181	9.562	0.220
7140	9.392	0.355	9.150	9.132	9.072	9.405	0.179	0.022	0.041
ucac	12.649	0.633	11.403	11.098	11.010	12.480	0.847	0.058	0.108
Non-members									
3004	10.428	0.354	9.927	9.793	9.746	10.526	0.466	0.024	0.045
3423	10.932	0.508	10.013	9.673	9.674	10.813	0.668	0.001	0.003
4294	6.813	0.207	6.478	6.470	6.513	6.573	0.018

Notes. ^a From the APASS catalogue (Henden et al. 2016). ^b From the 2MASS catalogue (Skrutskie et al. 2006). ^c From the *Gaia*-DR3 catalogue (Gaia Collaboration et al. 2022). * Scaled from the V and $(B - V)$ values of Kharchenko & Roeser (2009) and the relation proposed in the present work.

**Fig. A.2.** The same as in Fig. A.1 but with the photometric values.

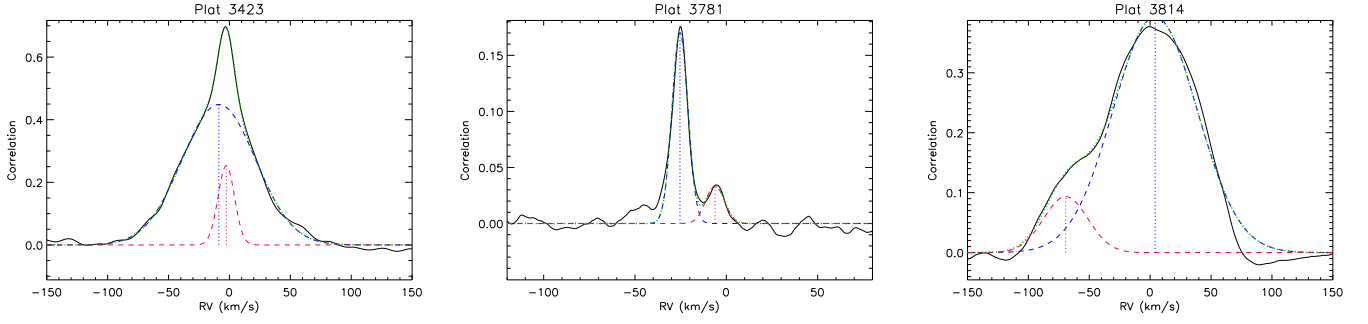


Fig. A.3. Cross-correlation functions (CCFs) for the three newly discovered spectroscopic binaries. In each box, the CCF is depicted with a full black line. The two-Gaussian fit is over-plotted with a dotted green line, while the Gaussians reproducing the primary (more luminous) and secondary components are plotted with dashed blue and red lines, respectively.

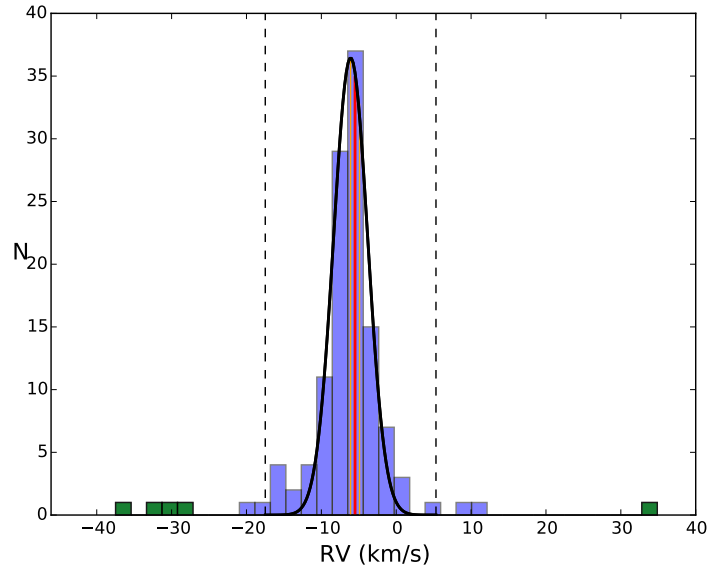
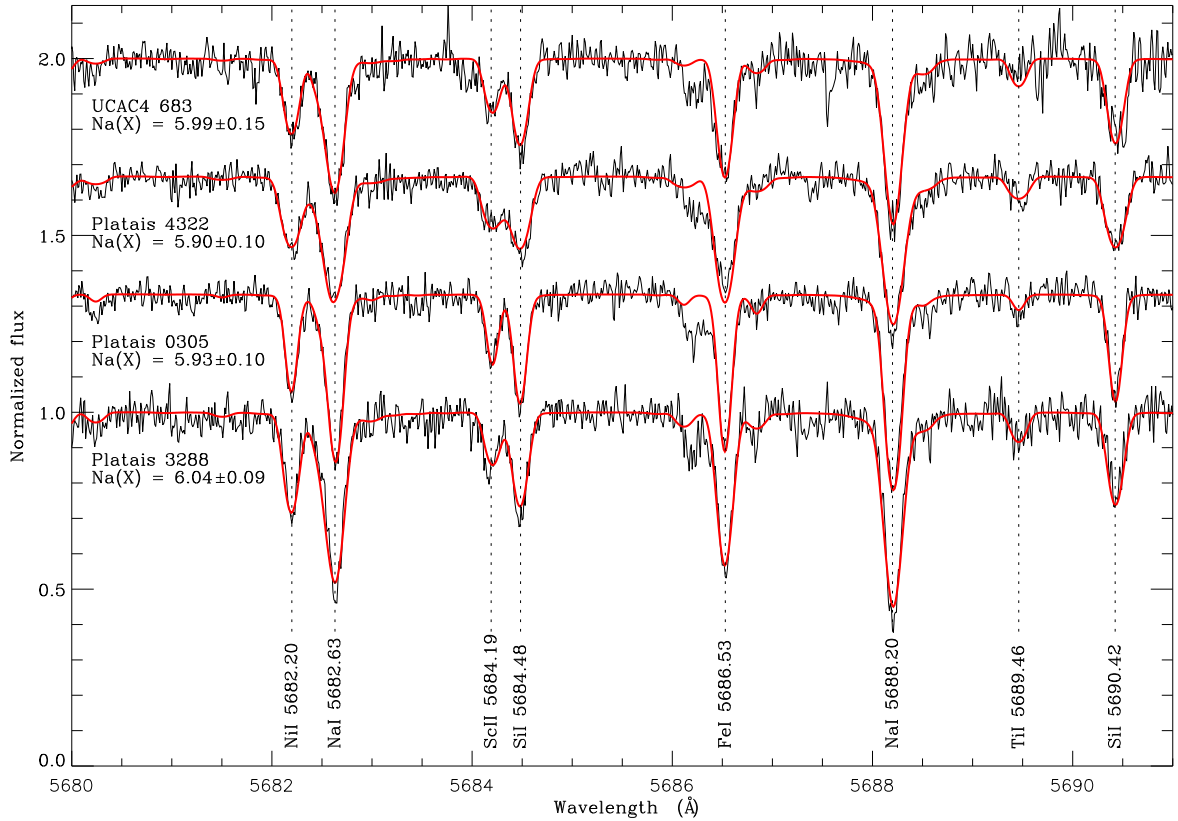


Fig. A.4. Distribution of the *Gaia* RV for the likely candidate members selected on the basis of the astrometric and photometric criteria explained in the text (blue histogram). The average RV for the cluster, found by the Gaussian fitting (solid black line), peaks at $-6.1 \pm 2.3 \text{ km s}^{-1}$. This value agrees closely with the RV obtained from the stars observed spectroscopically in this work (red line for the average value and orange lines for its uncertainty). The 5σ boundary is marked by dashed lines. The five objects that lie outside this boundary, taking into account their errors, have been represented with a green histogram and are considered non-members.

Table A.3. Chemical abundances, expressed as $A(X)=\log[n(X)/n(H)]+12$, for the cool stars observed in this work.

X	0305	3004*	3061	3288	3311	4322	4438	5609	ucac
C	8.52±0.10	8.78±0.12	8.70±0.09	8.49±0.12	8.26±0.15	8.31±0.11	8.49±0.10	8.53±0.07	8.70±0.14
Na	5.93±0.10	6.02±0.10	5.70±0.10	6.04±0.09	5.73±0.14	5.90±0.10	6.00±0.13	6.06±0.12	5.99±0.15
Mg	7.56±0.10	7.61±0.10	7.63±0.10	7.69±0.10	7.63±0.15	7.62±0.10	7.72±0.15	7.77±0.20	7.67±0.10
Al	6.53±0.10	6.61±0.15	6.32±0.10	6.59±0.10	6.47±0.10	6.60±0.10	6.54±0.09	6.50±0.12	6.62±0.10
Si	7.39±0.12	7.85±0.11	7.39±0.08	7.53±0.10	7.62±0.10	7.68±0.11	7.63±0.09	7.59±0.10	7.54±0.12
S	7.37±0.11	7.57±0.14	7.22±0.11	7.54±0.10	7.45±0.09	7.48±0.10	7.41±0.07	7.54±0.07	7.61±0.10
Ca	6.62±0.10	6.64±0.05	6.35±0.11	6.63±0.08	6.44±0.03	6.51±0.11	6.53±0.09	6.59±0.09	6.61±0.08
Sc	3.28±0.09	3.49±0.12	3.36±0.05	3.36±0.10	3.17±0.07	3.28±0.10	3.39±0.10	3.29±0.09	3.33±0.10
Ti	4.93±0.12	5.21±0.10	4.63±0.13	5.00±0.09	5.17±0.09	4.81±0.11	5.02±0.08	5.18±0.10	4.83±0.10
V	4.13±0.08	4.30±0.10	4.15±0.17	4.23±0.08	4.27±0.04	4.17±0.05	4.22±0.10	4.23±0.10	4.24±0.09
Cr	5.79±0.04	5.89±0.10	5.57±0.13	5.86±0.10	5.80±0.06	5.78±0.04	5.79±0.11	5.75±0.08	5.84±0.10
Mn	5.48±0.10	5.65±0.10	5.43±0.10	5.59±0.10	5.35±0.05	5.49±0.12	5.58±0.06	5.62±0.10	5.59±0.10
Fe	7.48±0.13	7.53±0.14	7.05±0.10	7.58±0.12	7.51±0.11	7.48±0.12	7.52±0.17	7.33±0.12	7.51±0.10
Co	4.86±0.14	5.25±0.10	4.76±0.13	4.98±0.12	4.95±0.18	4.91±0.10	4.97±0.10	5.07±0.10	4.97±0.10
Ni	6.16±0.12	6.39±0.05	6.06±0.12	6.24±0.11	6.26±0.09	6.16±0.13	6.25±0.13	6.28±0.10	6.21±0.11
Cu	4.34±0.10	4.48±0.10	4.21±0.10	4.36±0.10	4.36±0.10	4.27±0.10	4.33±0.10	4.50±0.10	4.34±0.10
Zn	4.28±0.18	4.80±0.10	5.00±0.20	4.55±0.10	4.76±0.30	4.35±0.10	4.72±0.10	4.72±0.10	4.60±0.10
Sr	3.30±0.09	3.30±0.10	3.24±0.10	3.33±0.10	3.11±0.08	3.32±0.10	3.21±0.10	3.20±0.10	3.29±0.15
Y	2.47±0.08	2.46±0.10	2.39±0.10	2.48±0.10	2.50±0.09	2.50±0.11	2.46±0.10	2.46±0.12	2.50±0.10
Zr	2.93±0.10	2.93±0.25	2.75±0.10	2.90±0.10	2.74±0.13	2.91±0.10	2.85±0.10	2.80±0.07	2.97±0.10
Ba	2.60±0.06	2.93±0.10	2.35±0.09	2.63±0.08	2.63±0.17	2.52±0.10	2.54±0.10	2.58±0.14	2.55±0.08

* Non-member.

**Fig. A.5.** Example of spectral synthesis for the stars in our sample with lower $v \sin i$. The two most intense spectral features in this range (5680–5700 Å) correspond to Na I lines, the abundance of which is shown.